Graphyne-based membrane as a promising candidate for Li-Battery electrodes protection Insight from atomistic simulations

Lemaalem, Mohammed; Khossossi, Nabil; Bouder, Gaelle; Dey, Poulumi; Carbonnière, Philippe

DOI
10.1016/j.jpowsour.2023.233482

Publication date
2023

Document Version
Final published version

Published in
Journal of Power Sources

Journal of Power Sources 581 (2023) 233482

Contents lists available at ScienceDirect

Journal of Power Sources

journal homepage: www.elsevier.com/locate/jpowsour

Graphyne-based membrane as a promising candidate for Li-Battery electrodes protection: Insight from atomistic simulations

Mohammed Lemaalem [a,*], Nabil Khossossi [b,*], Gaelle Bouder [a], Poulumi Dey [b], Philippe Carbonnière [a,*]

[a] University of Pau and Pays de l'Adour, E2S UPPA, CNRS, IPREM UMR5254, Institut des Sciences Analytiques et de Physico-chimie pour l'Environnement et les Matériaux, Hélioparc, 64000 Pau, France

[b] Department of Materials Science and Engineering, Faculty of Mechanical, Maritime and Materials Engineering, Delft University of Technology, Mekelweg 2, 2628 CD Delft, The Netherlands

HIGHLIGHTS

- Graphyne-n for battery electrode protection are explored via MD and DFT simulations.
- Graphtriyne showed high Li^+ permeability and enabled electrolyte/electrode contact.
- Graphyne exhibited lower Li^+ permeability but prevented electrode/electrolyte contact.
- Graphyne and graphdiyne assure Li-battery electrode safety and control the Li^+ flow.

ARTICLE INFO

Keywords:
2D nanoporous graphyne-n
Electrodes protection
Li-metal battery

ABSTRACT

All-solid electrolytes could lead to a technological breakthrough in the performance of all-solid-state batteries when combined with a lithium-metal anode. However, the use of a lithium-metal anode presents several challenges, such as dendrite growth, interface electrochemical stability, formation and propagation of cracks, and delamination of the electrode/electrolyte interfaces. This work aims to explore the effectiveness of using newly synthesized 2D graphyne-based membranes (namely graphyne, graphdiyne, and graphtriyne) for electrode protection in a solid polymer electrolyte battery through first-principle calculations, nudged elastic band method, and classical molecular dynamics simulation. Specifically, we aim to investigate the effectiveness of these membranes in mitigating the aforementioned challenges. A high external electric field of up to 0.5 V/Å, 0.75 V/Å, and 1 V/Å was applied to accelerate the ions diffusion process. The adsorption energies, charge transfer, and in-plane/out-plane diffusion of single lithium on graphyne-based surfaces were investigated. Afterward, we calculated and compared the Li^+ permeability, the electrolyte molecules' rejection efficiency, and the intrinsic properties of graphyne-based nanoporous membranes. Our findings show that both graphyne and graphdiyne surfaces effectively permit Li^+ intercalation while preventing other electrolyte molecules from reaching the electrodes.

1. Introduction

High-power all-solid-state Li-Batteries (AllSSLiBs) for energy storage are probably the most exciting prospect for a safe energy source for electric vehicles (EVs) [1–5]. Indeed, they offer all the upsides that batteries should provide for the automotive market, namely short charging time, high energy density, and safe operation. The coordinated effort made by industrial and academic researchers towards enhancing all-solid-state battery technology makes their arrival on the market conceivable [6–9]. Thus, they will be used in several sectors, notably where energy density represents a limit [10–12]. Indeed, solid-state Li batteries with a Li metal anode, which have a high energy density with respect to other electrode materials, will make it possible to enhance battery autonomy, i.e., reduce the battery size, and now seem to be the future of the automotive market and mobility as a whole [13,14]. However, AllSSLiBs have some downsides limiting their large commercialization until now. The problems limiting the AllSSLiBs integration in EVs predominantly occur in the interface between electrolyte and electrodes [15,16]. The electrolyte–electrode interface presents three

* Corresponding authors.
E-mail addresses: mohammed.lemaalem@univ-pau.fr (M. Lemaalem), n.khossossi@tudelft.nl (N. Khossossi), philippe.carbonniere@univ-pau.fr (P. Carbonnière).

https://doi.org/10.1016/j.jpowsour.2023.233482
Received 31 May 2023; Received in revised form 7 July 2023; Accepted 2 August 2023
Available online 18 August 2023

distinguished challenges [17]. The first challenge is dendrite growth from the anode to the cathode, which eventually causes the battery to short circuit [18–20]. The second challenge is the interface's electrochemical stability. The interactions in the interface between solid electrolytes and electrodes, especially with metal anode electrodes, can lead to the dissociation of electrolyte molecules and the formation of new molecules that may impede the transport of ions. This can hinder the battery's performance [21–24]. The third challenge is the dependence of ionic conductivity on the structural features that occur in the interface anode/electrolyte and cathode/electrolyte [25–30]. The contact cathode/electrolyte is affected by the stresses developed during electrochemical cycling, leading to the formation and propagation of cracks and delamination of interfaces [31–34]. Yet, the naturally formed solid electrolyte interphases (SEIs) films in situ, such as Li-F, can stabilize the Li-electrolyte interface [35,36], which are supposed to prevent Li dendrite growth. They are inefficient for the battery's long life cycle because of their uncontrollable structure [37]. Recently, researchers have focused more and more on designing and developing artificial SEI layers to meet the electrode/electrolyte interface challenges in AllSSLiBs [38–40]. Artificial SEIs are primarily developed to prevent electrolyte decomposition and dendrite formation, to restrain the electrode volume changes, and to ensure uniform Li-ion intercalation [37,41]. The developed artificial SEI, which can be organic or inorganic, should have high mechanical strength and should permit Li^+ diffusion. In addition, SEI should be electrochemically stable and compatible with different electrolytes to achieve a long life cycle [42,43]. In this contest, alginate, PAA, PVDF, and organic alkoxide-based artificial SEI [44,45] are introduced based on their high mechanical strength and adhesion to the Li metal anode. Carbon-nano-tube sponge (CNT-sponge) [46,47], vertically aligned carbon nanofiber [48–50], and carbon cloth [51,52] are promising materials as 3D current collectors. They are uncomplicated to fabricate and characterized by high ionic conductivity, flexibility, lightweight, and a high ability to suppress the growth of Li anode dendrites. Polymers, such as Polypropylene (PP), Polyacrylonitrile (PAN), and polyvinylidene difluoride (PVDF) [53–55], and carbon nanotubes (CNT) [56,57], are among the most commonly used materials in developing multilayer functional membranes as interphases between electrodes and electrolytes for high-power Li-metal batteries. They can not only prevent dendrite growth but also improve the cathode electrochemical properties [58,59]. They permit Li^+ diffusion through their pores. However, they can allow electrolyte molecules to penetrate [60].

In this work, we propose an alternative solution that prevents direct contact between electrolytes and electrodes by coating the electrodes with graphyne-n (n = 1, 2, 3) layers that are permeable to small cations, such as Li^+ and Na^+. The structural models of graphyne (n = 1), graphdiyne (n = 2), and graphtriyne (n = 3) were first proposed by R. H. Baughman et al. [61]. They are 2D carbon allotropes composed of acetylenic linkages (sp-) and benzene (aromatic rings) (sp^2-hybridized carbon atoms) [62]. Graphyne is a one-atom-thick planar sheet. Its synthesis started in 2018 using interfacial methods, mechanochemical, ultrasonication, and dynamic covalent chemistry [63–66]. In late 2022, Barua et al. reported a simple and high-yield synthesis of graphyne via a one-pot Sonogashira cross-linking reaction [67]. Graphdiyne, synthesized since 2010 [68], is the most stable non-natural carbon allotrope containing diacetylene bonds [69]. Because of its porous structure containing triangular pores of sizes 3.94 Å, 5.42 Å [70], and 6.69 Å [71] for graphyne, graphdiyne, and graphtriyne, respectively, and conjugated carbons, graphyne-n provides storage sites and diffusion pathways for small ions such as Li^+. Thus, the Li^+ can diffuse in parallel and perpendicular directions to the graphyne-n layers [72–74]. These properties make graphyne-n a promising 2D material in energy-storage batteries [72,73,75–80].

Graphdiyne is tested as an electrode, where the graphdiyne layers are positioned perpendicular to the metal anode surface [73,78,79]. It has been demonstrated that the specific capacities and lithiation potentials are enhanced [78], and the intercalation density of Li^+ in graphdiyne is more important with respect to graphyne [73,79]. Experimentally, in a battery model proposed by Huang et al. [81], graphdiyne was synthesized in situ through cross-coupling and used as a Li^+ storage electrode. In this model, graphdiyne is used without additives or binders. However, the battery demonstrates a high capacity of up to 520 $mAhg^{-1}$, long cycling stability of up to 400 cycles, and good rate performance with a current density of 500 mAg^{-1} [81–83]. Nevertheless, the life cycles of solid-state batteries currently in the test phase are ten times less than those of other lithium-ion technologies, such as the Lithium Iron Phosphate (LFP) batteries, which exceed 4000 charge cycles [84,85].

We coupled molecular dynamics simulations (MD) and density functional theory calculations (DFT) to reveal the role of graphyne-n. They are introduced as an artificial interphase between the electrode and electrolyte to act as a buffer for the electrodes. This helps prevent interaction between the electrolyte and electrodes. We also probed how the electrolyte molecules behave near the graphyne-n layers. The studied battery model consists of solid polymer electrolytes (SPEs) delimited by two graphyne-n surfaces, where each surface is composed of four layers of a graphyne-n sheet (see Fig. 1), with n = 1, 2, or 3. The SPEs model is composed of 12 polyvinylidene difluoride (PVDF) chains, where each chain contains 150 carbons. The polymer has a molecular weight of 40% lithium bis(fluorosulfonyl)imide (LiFSI) salt, which is equivalent to 14 carbons/LiFSI. Additionally, fluoroethylene carbonate (FEC) is added as an additive with the molar fraction n(FEC)/n(LiFSI) = 1. From MD simulations, we characterized the graphyne-n selectivity towards the electrolyte components (Li^+ cations, FSI^- anions, FEC solvent, and PVDF polymer chains) under a high voltage that can be modeled by the application of a high electric field [86,87]. From DFT calculations, we characterized the local diffusion behavior of the different electrolyte components on a graphyne-n monolayer. We expect that introducing graphyne-n layers as an artificial interphase between the electrolyte and electrodes could reduce the electrolyte–electrode contact, improving battery stability. Yet, they permit the Li^+ cations to intercalate from the cathode to the anode and vice versa during charge–discharge cycles.

2. Results and discussion

Initially, we fully optimized the geometric structure of graphyne-based membranes, as illustrated in the right panel of Fig. 1. After full optimization, the geometry structure of all three considered membranes maintains their graphene-like planar structure. Based on our calculations, the distance between the two nearest neighbor hexagonal carbon rings are found to be 6.877, 9.355, 11.924 Å which also represents the lattice constant simulating the rhombus unit cell of graphyne, graphdiyne, and graphtriyne, respectively. The calculated pore sizes are of 3.97 Å for graphyne, 5.40 Å for graphdiyne, and 6.88 Å for graphtriyne align closely with the reported values of 3.94 Å for graphyne [70], 5.42 Å for graphdiyne [70], and 6.69 Å for graphtriyne [71]. The bond length of two carbon atoms can be considered as an indicator for determining the type of bond. Basically, the bond-length of single σ-bond is about 1.47 Å, whereas both double (σ+π)- and triple (σ+2π)-bonds shrink respectively to 1.38 Å and 1.21 Å. It is worthy of mention that in this case, π denotes a localized π-orbital. Once a large delocalized π-orbital gets involved in the bond, the bond-length of the corresponding bond becomes a bit longer. In the hexagonal carbon rings of graphyne, the bond length is 1.43 Å, which occurs in between single and double bonds, corresponding to a (σ+π)-bond, which is quite similar to that of a conventional graphene monolayer, which is about 1.42 Å. The bond length in the inner carbon chain is estimated to be about 1.22 Å, which is quite close to the triple bond. Therefore, owing to the trivalent character of C-atom, the bond linking the hexagonal ring and C-chain is expected to be a single σ-bond. Nevertheless, the bond length is 1.41 Å, which is shorter with respect to a typical C–C bond which is 1.47 Å, which can be understood based on the electrostatic force between two C-sites.

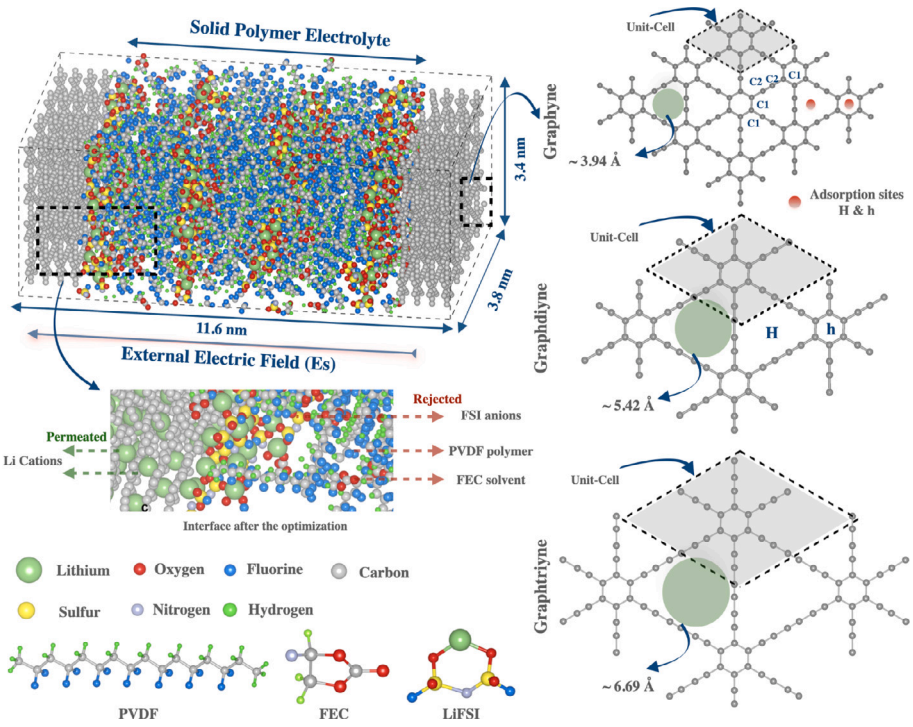

Fig. 1. Snapshot of an initial configuration, where the volume of the polymer electrolyte is pre-equilibrated under room temperature and ambient pressure (T = 300 K, P = 1 bar) before adding four graphyne-n layers on two opposite sides perpendicular to the electric field direction. For simplicity, the anode and cathode are replaced by reflective walls during MD simulations. The zoomed-inset snapshot shows Li^+ cations passed through the graphyne nanopores as other electrolyte molecules rejected during MD simulation under the application of a high external electric field.

2.1. Li^+ permeability and electrolyte molecules rejection efficiency calculated from MD simulation

Qualitative results can be seen in Fig. S1, which depicts snapshots of the performed MD simulations. The figure shows that only Li^+ can penetrate the graphyne layer under a high external electric field application. We presented the visualizations of the nine simulated cases as supplementary movies of 1 ns MD simulation depicting the Li^+ intercalation under the application of an external electric field directed from the cathode to the anode (cf. supplementary information). Moreover, from the MD simulation trajectory analyses, in agreement with previous studies [88,89], the graphyne-n interlayer distance from the present MD simulations is around 3.7 ± 0.1 Å, which permits the parallel diffusion of Li^+ between the graphyne-n layers.

For a quantitative investigation of graphyne-n selectivity, we calculate the Li^+ permeability and the rejection percentages of other molecules. In the present study, solvent, polymer, and counterion rejection (R) are defined as the percentage of molecules that do not pass across the graphyne-n layers after a simulation time of δ t = 1 ns, $R = \frac{N_T - N_p}{N_T * \delta t} * 100$, with N_T the total number of molecules in the simulation box (feed molecules) and N_p the number of permeated molecules. Besides, to adjust the effect of the applied external electric field (E) and the area of the graphyne-n membranes (S), Li^+ cation permeability was calculated. The Li^+ permeability (P) is calculated as:

$$P = \frac{F_{eff}}{E * t} \tag{1}$$

Where F_{eff} is the effective flux, defined as $F_{eff} = \frac{F}{S}$. The flux ($F = \frac{N_p}{\delta t}$) represents the number of cations that pass across the membrane surface N_p during a simulation time of δ t = 1 ns. The applied external electric field was E = 0.5 V/Å, E = 0.75 V/Å, and E = 1 V/Å. In molecular dynamics simulations of nano-batteries, the use of a high external electric field of up to 1 V/Å is crucial for accurately modeling battery behavior and predicting their performance [86,87]. Indeed, applying a high electric field can enhance ion transport within the battery, leading to improved charging and discharging rates.

MD simulation results of cation permeability and molecule rejection are presented in Fig. 2. Accordingly, the Li^+ permeability across graphdiyne and graphtriyne was higher than that of graphyne. This is due to the fact that the size of nanopores on graphdiyne and graphtriyne is higher than on graphyne.

To evaluate the influence of the applied external electric field (E) on Li^+ permeability and the rejection of other electrolytic molecules, four layers of graphyne, graphdiyne, and graphtriyne were used to protect the electrodes in an all solid state battery model using solid polyelectrolyte, as described in the above section. Three applied external electric fields, E = 0.5, 0.75, and 1 V/Å (see Fig. 2), were utilized. By increasing the applied electric field (E), the ions were exposed to a greater force towards the membrane and would easily pass through the nanopores. The cations are oriented in the direction of the electric field, and the anions are oriented in the opposite direction. The Li^+ flux (the number of Li^+ ions passing through the membrane within 1 ns) increased almost linearly. The FSI^- rejection decreased for graphdiyne and graphtriyne to 60% and 4%, respectively, and remained unchanged at 100% for graphyne, for the highest applied electric field E = 1 V/Å. The solvent rejection decreased slightly for graphdiyne and graphtriyne, and remained unchanged at 100% for graphyne. The PVDF rejection remained unchanged for the three graphyne-n membranes.

As shown in Fig. 2a, by increasing E, the Li^+ flow rate (flux) increased. In Fig. 2b, Li^+ permeability is presented after adjusting for the effects of E and the area of the membrane. Considering that the increase of E is more prominent than the increase of the Li^+ flux (Fig. 2a), the slight increase in Li^+ permeability in Fig. 2b from E = 0.75 V/Å to E = 1 V/Å compared to the increase in permeability from E = 0.5 V/Å to E = 0.75 V/Å is justifiable. According to Fig. 2a, b, c, and d, graphyne is more efficient than graphdiyne and graphtriyne membranes for electrode protection at all the applied E values. At the applied electric field of 1 V/Å, the advantage of using graphyne is obvious. The Li^+ permeability values are comparable to those obtained

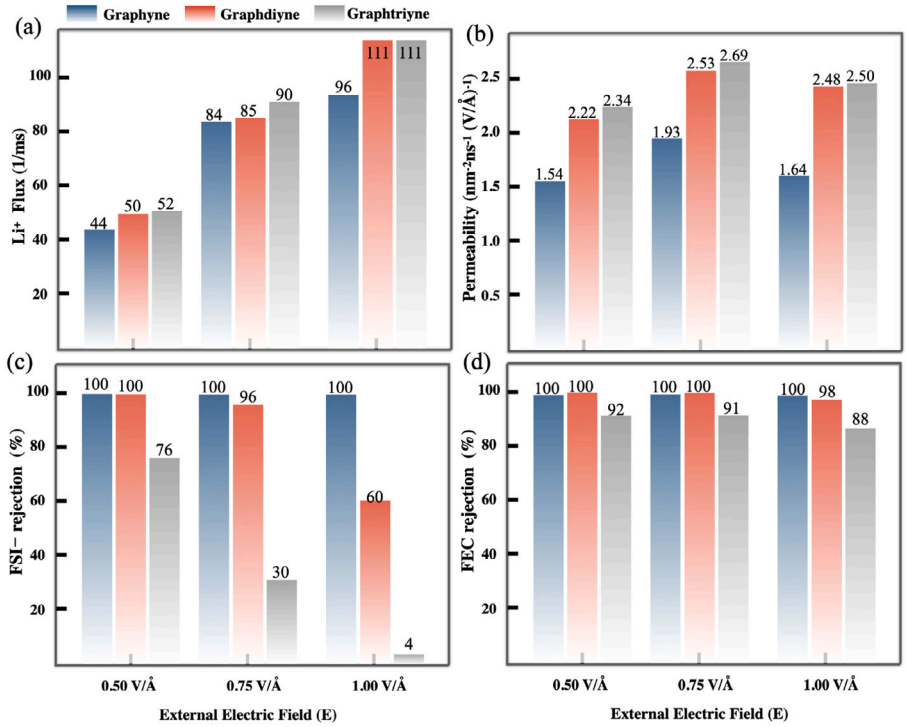

Fig. 2. (a) Li^+ flux (flow rate) as a function of applied external electric field (E), (b) Li^+ effective permeability per area for graphyne-n membrane (n = 1, 2, 3), (c) and (d) electrolyte molecules, FSI^- and FEC, rejection efficiencies as a function of the applied external electric field.

for graphdiyne and graphtriyne, and the rejection of other electrolyte molecules is 100%, for an applied E from 0.5 to 1 V/Å.

From the NVT MD simulations of the proposed nanobattery model under high voltage (high external electric field) application, the solvent and anions can pass through the graphdiyne and graphtriyne membranes, resulting in a small rejection percentage of electrolytic molecules. A conventional notion in the all-solid-state battery field is that fast charging and battery stability are the main factors. Then, even though we show that graphtriyne and graphdiyne can achieve high theoretical Li^+ permeability, anions and solvent molecules can permeate through them and interact with the electrodes.

Interestingly, our MD simulations show that the 2D graphyne sheet can provide fast charging (accumulation of Li^+ cations in the anode) and high efficiency for battery stability (preventing electrolyte/electrode contact). Thereby, graphyne is a potential candidate as an ideal electrode cover. Graphyne is less affected by high external electric field application, but the graphdiyne and graphtriyne membrane structures become defective. These defective membrane structures of graphdiyne and graphtriyne, under stress generated by the flux of molecules, can be related to their mechanical stiffness, which will be discussed in the next section.

Fig. 3a shows the Li^+ trajectory lines during a 1 ns MD simulation. Herein, we created the Li^+ trajectories painted in black, following the path of the selected Li^+ cations for E = 1 V/Å. We observed the same behavior for E = 0.5 and E = 0.75 V/Å. These illustrations also provide a qualitative result of the ability of graphyne-n to pass Li^+ cations through its pores and store them. Inside the graphyne-n membranes, the trajectory lines of Li^+ are not straight, as in the electrolyte. Especially inside graphyne, their trajectories are solenoid-like. The relatively large pores of graphdiyne and graphtriyne, compared to graphyne, make perpendicular diffusion of Li^+ easier. Differently, Li^+ prefers to diffuse parallel to graphyne. However, the graphyne pores also permit the perpendicular diffusion of Li^+. These diffusion types are related to the Li^+-membrane interaction, which we quantified from the g(r) curves as depicted in Fig. 3b, c, and d. Accordingly, the interaction of Li^+-graphyne is more important than those of Li^+-graphdiyne and Li^+-graphtriyne. Therefore, Li^+ adheres to the membrane layers. Hence, graphyne can be used as a host anode to store Li^+. We note that the Li^+-membrane interaction increases proportionally to the magnitude of the applied electric field (see Fig. 3b, c, and d). This increase is explained by the increase of Li^+ flux towards the graphyne-n layers, proportionally to E (Fig. 2a). We also noted that the Li^+-graphdiyne interaction is slightly less than the Li^+-graphtriyne interaction.

Further investigations of the interaction between lithium and graphyne are conducted using density functional theory (DFT) calculations along with the climbing image nudged elastic band (CI-NEB) approach. These methods allowed for a detailed analysis of the binding energy, which served as an important measure of the interaction strength between Li and the 2D surfaces of graphyne, graphdiyne, and graphtriyne. To conduct the study, a large super-cell of approximately 2 × 2 × 1 2D lattices was used as the anchoring material. We examined the binding strength of Li atoms and electrolyte molecules, including FSI^-, FEC, and PVDF. To determine the energetically favored binding site, we fully optimized various orientations and directions of Li and electrolyte molecules at possible binding sites on the 2D surfaces of graphyne, graphdiyne, and graphtriyne. The principle is derived according to the binding strength formula given below:

$$E_b = E_{Surface} + E_M - E_{M@Surface} \quad (M = Li/FSI^-/FEC/PVDF) \quad (2)$$

Wherein $E_{M@Surface}$ and $E_{Surface}$ refer to the total free energies of 2D graphyne, graphdiyne, and graphtriyne surfaces after and before the adsorption of Li atoms and electrolyte molecules, respectively. E_M refers to the average total energy of Li/FSI^-/FEC/PVDF in the bulk reference state with a simulation box of lattice constant set to 25 Å. Typically, the use of the vdW-correction significantly affects the binding strengths; therefore, the energies have been evaluated in the presence of vdW-correction [90,91]. In this context, the stronger the binding strength, the more stable the binding configuration. This indicates an exothermic reaction and a scattering distribution of the adsorbed Li and electrolyte molecules, rather than clustering. This helps to avoid issues that may arise from the formation of Li-dendrites or

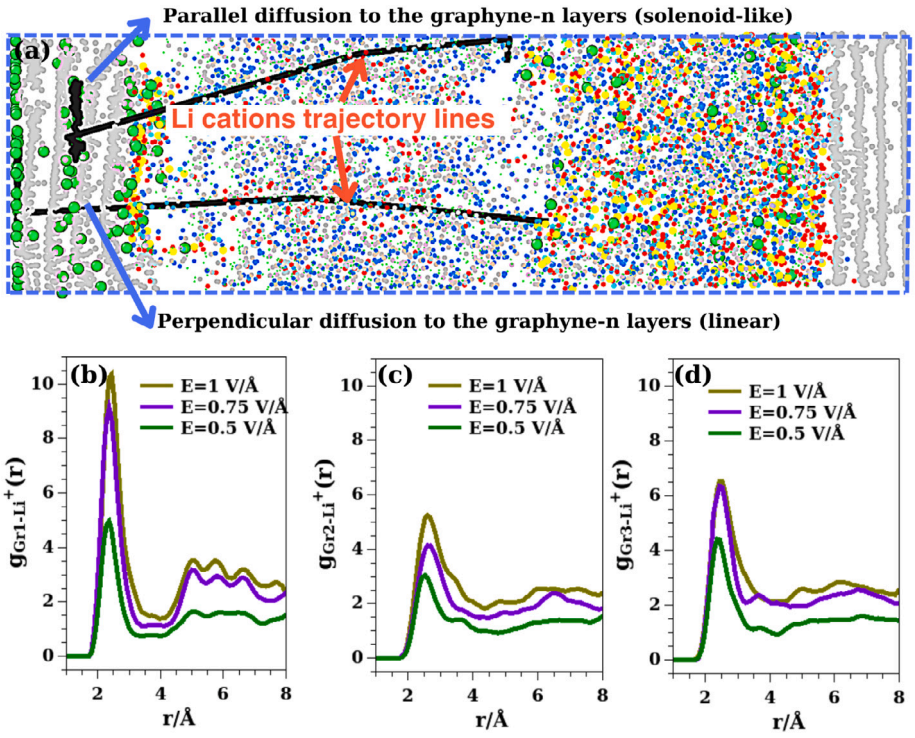

Fig. 3. Effect of graphyne-Li^+ interaction on the diffusion pathway of Li^+. (a), two trajectory lines of two picked Li^+ cations, where the perpendicular and parallel diffusion pathways in graphdiyne are highlighted on the simulation box. Similar visualizations are noted for the Li^+ trajectory analyses in graphyne and graphtriyne (data not shown). From (b) to (d), the radial distribution function, g(r), of Li^+-graphyne-n, (n = 1, 2, 3), (b) $g_{Li^+-graphyne}$ (r) (g_{Gr1-Li^+}(r)), (c) $g_{Li^+-graphdiyne}$(r) (g_{Gr2-Li^+}(r)), and (d) $g_{Li^+-graphtriyne}$(r) (g_{Gr3-Li^+}(r)) calculated for different values of the applied external electric field (E).

metal clusters during the charge–discharge process. Within the binding active sites and orientations explored, the most stable configurations with the lowest energy strength are illustrated in Fig. 4. The binding strengths of Li atoms and the electrolyte molecules adsorbed on the three considered graphyne surfaces are outlined in Table 1. As depicted in Fig. 4, two distinct binding sites are possible for the adsorption of Li atoms and FSI^-/FEC/PVDF clusters: above the center of carbon hexagons and above the center of carbon triangular-like pores. The binding energy of the Li-atom was calculated to be 3.28, 2.63, and 1.85 eV at the H-site of graphyne, graphdiyne, and graphtryine, respectively. The binding height decreases as a function of the diameter of the pore, which is an important factor in assessing the applicability of anchoring graphyne-based membranes for Li-metal batteries.

The binding energy of lithium atoms on 2D surfaces made of graphyne, graphdiyne, and graphtriyne was calculated and found to be significantly higher than that of the lithium dimer (0.94 eV), small lithium clusters (< 1.47 eV), and lithium in its bulk reference state (1.61 eV) [92]. The current findings suggest that the energy required for Li clustering during the processes of lithiation and delithiation would make it unfavorable, thus impeding its occurrence. It is interesting to note that the adsorption of more than one lithium atom at the triangular pore of graphdiyne and graphtriyne leads to their extrusion out of plane and to their separation from each other. This supports the fact that the Li atoms can be scattered well on these surfaces without clustering. We further explicitly verified that the configuration of a single Li atom adsorbed in the triangular-like pore is more stable with respect to the corresponding configuration with multiple Li atoms. This may be ascribed to the Coulomb repulsion occurring between the positively charged Li^+ ions, which is driven by the charge transfer from Li atoms to the surface of graphyne-based monolayers. Additionally, the adsorption of other electrolytic compounds has been investigated. The binding strengths of FSI^- anions, FEC solvent, and PVDF polymer chains on the considered surfaces are summarized in Table 1. It has been found that the FSI^- and FEC solvents adsorbed right above the triangular-like pores and parallel to the surface, with the shortest adsorption distance ranging from 0.97 to 1.55 Å. The binding energy of the FSI^- molecule adsorbed on graphyne-based surfaces decreases with an increase in pore size.

Table 1
Computed binding strength of Li and electrolyte molecules on the studied graphyne surfaces using DFT-D3, shortest binding height, charge transfer ΔQ ($|e|$)[a] between molecules and the anchoring surfaces.

2D Materials	Li/Electrolytes molecules	E_b (eV)	ΔQ (|e|)	h (Å)
Graphyne	Li	3.279	+0.436	0.873
	FSI^-	2.112	+0.572	1.383
	FEC	0.682	+0.417	1.546
	PVDF	0.076	−0.083	2.694
Graphdiyne	Li	2.063	+0.819	0.072
	FSI^-	1.627	+0.631	1.209
	FEC	0.816	+0.460	1.546
	PVDF	0.152	+0.128	1.925
Graphtriyne	Li	1.851	+0.906	0.005
	FSI^-	1.108	+0.726	0.973
	FEC	0.729	+0.491	1.046
	PVDF	0.208	+0.313	1.872

[a] $\Delta Q > 0$ reveals the electrons transfer from Li or electrolyte molecules to the graphyne-based surfaces.

The further elaboration of advanced and high-efficiency rechargeable Li-metal batteries is critically dependent on the applicability of Li-battery electrode protection, notably throughout the processes of charging and discharging. This is mainly characterized by both the kinetic properties of dilute Li-ion diffusion as well as electron transfer from Li-atom to the surface. Hence, the Bader charge analysis of a single Li atom and electrolyte molecules adsorbed on graphyne-based surfaces has been performed, and the results are summarized in Table 1. It can be clearly seen from our results that graphyne, graphdiyne, and graphtriyne gain a charge from the Li atom and electrolyte molecules.

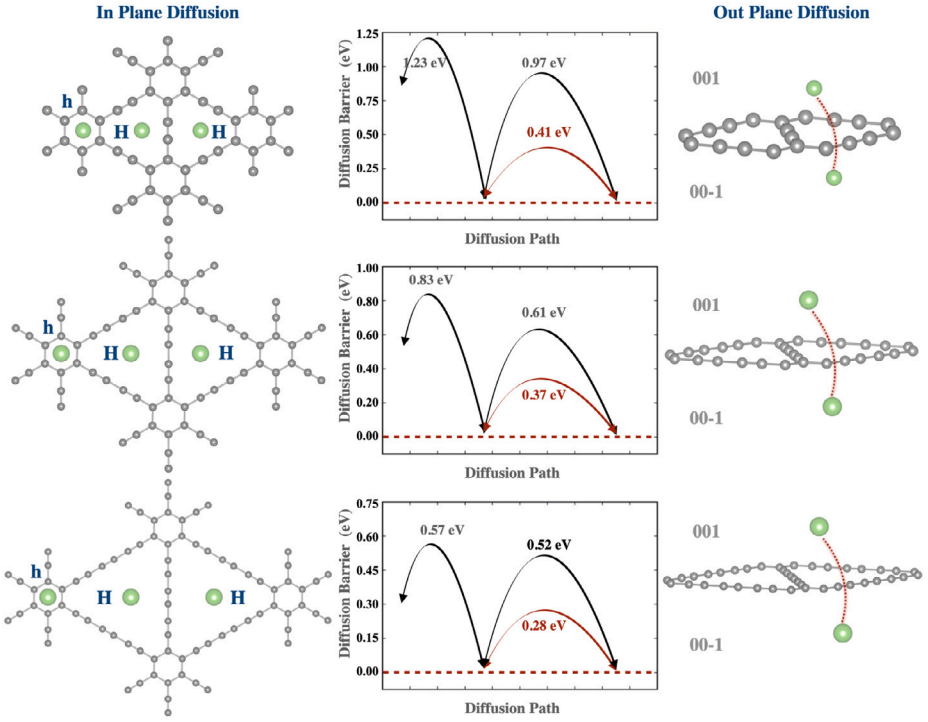

Fig. 4. Two different Li-diffusion pathways on in-plane and out-plane Graphyne-based surfaces along with their corresponding diffusion barrier profiles.

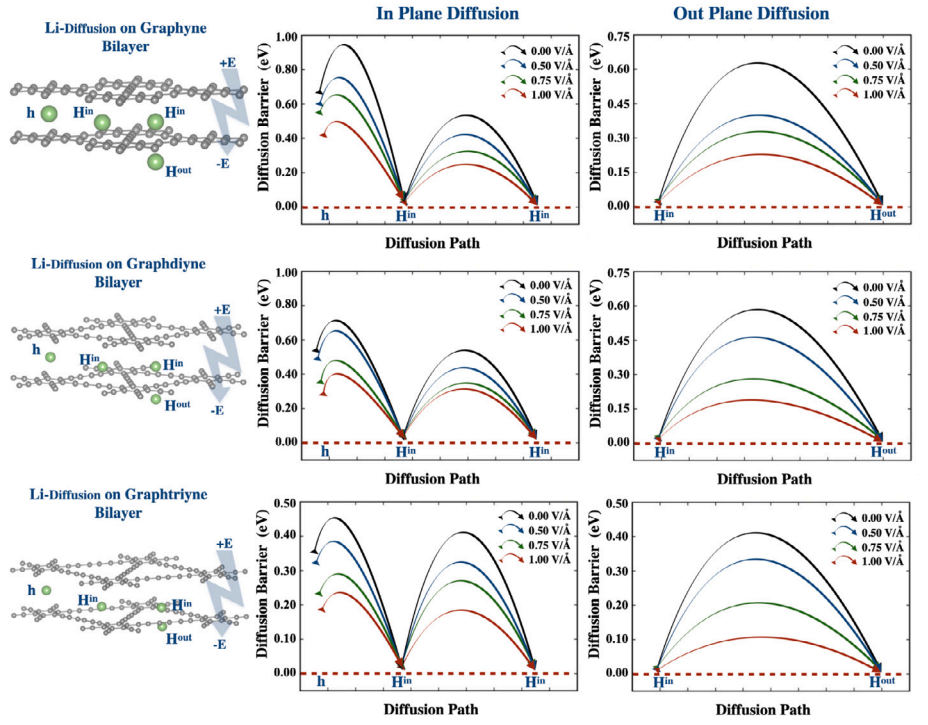

Fig. 5. Schematic illustration of Li-diffusion pathways on in-plane and out-plane bilayer Graphyne-based surfaces along with their corresponding diffusion barrier profiles.

It can also be mentioned that the contrasting signs of simulated charge transfer in PVDF with graphyne, graphdiyne, and graphtriyne can be attributed to the electronic structure and chemical properties of these carbon allotropes. Graphyne, with its high electron density, tends to accept charge from PVDF, resulting in a negative charge transfer of −0.083. Conversely, graphdiyne and graphtriyne, with their unique sp- and sp^2-hybridized carbon arrangements, donate charge to PVDF, leading to a positive charge transfer of about +0.128 and +0.313, respectively. Thereby providing a fast and efficient exchange of electrons in the host materials during the complete adsorption–desorption cycle, and serving as a major factor in the high-rate capacity of Li-metal batteries. Furthermore, the Li migration pathways, along with the corresponding minimum energy profile, were determined through the CI-NEB method for a single Li atom diffusing on the surface of each material. In Fig. 4, the schematic illustration of both Li diffusion pathways considered in our study with their minimum energy is shown,

namely in-plane and out-of-plane Li diffusion. The two considered pathways consist of symmetrical Li diffusion from the most stable adsorption site, characterized by the highest binding strength, to the nearest adsorption site. The in-plane pathway involves migration of the Li atom between two nearest H-sites through the C–C bridge, followed by another pathway from H-site to h-site. In this case, it can be clearly noticed from Fig. 4 that the Li atom needs to exceed a minimum energy barrier of 0.97, 0.61, and 0.52 eV to diffuse towards the closest H-site on graphyne, graphdiyne, and graphtriyne, respectively. For the out-of-plane pathway, the Li-ion migrates across the triangular-like pore with a computed minimum energy barrier of 0.41, 0.37, and 0.28 eV with respect to graphyne, graphdiyne, and graphtriyne, respectively. These results are consistent with the binding energy values. The Li-diffusion energy barrier is inversely proportional to the triangular pore size. In addition, the diffusion of FSI^{-}, FEC, and PVDF on graphyne-based surfaces was also examined, and a similar trend was observed. Based on the analysis of these findings and in agreement with the MD simulation results presented in Fig. 3, it can be stated that our proposed graphyne-based surfaces provide fast and efficient lateral diffusion of Li and electrolyte molecules. Moreover, when comparing these outcomes, both graphyne and graphdiyne are expected to play a crucial role in protecting Li-battery electrodes. However, the surface of graphtriyne may allow some electrolyte molecules to pass through due to its larger triangular pores compared to other surfaces. In addition, the application of an external electric field is an effective strategy to modulate the kinetic properties of ultrathin nanomaterials [91,93]. The variation of Li-diffusion barrier profiles as a function of an external electric field was investigated. We have applied a transverse electric field varying from 0.0 V/Å to +1.0 V/Å, which acts as a staggered potential for the atomic arrangement on the surfaces. From Fig. 5, it can be seen that the external electric field enhances the Li diffusion through the aforementioned pathways.

2.2. Intrinsic properties of graphyne-n monolayers from MD simulations

Recent research has shown that the elastic modulus of the electrode material can play a vital role in preventing dendrite formation and growth. Indeed, a minimum modulus of 6.2 GPa has been suggested as a minimum requirement for suppressing dendrite growth [94]. Fig. 6 presents the stress–strain curves of the three considered graphyne-n obtained from uniaxial tensile deformation based on MD simulations, systematically compared to graphene. In agreement with previous studies [95–97], our MD simulations show that the graphyne-n sheets exhibit good mechanical strength. We note that graphyne exhibits superior mechanical properties than graphdiyne and graphtriyne due to the triple bonds between the sp hybridized carbon atoms in its planar structure, which unequivocally enhances its rigidity. Calculated mechanical properties for graphyne, graphdiyne, and graphtriyne monolayers are presented in Table 2. For comparison, we also calculated the Young's modulus of graphene, which was found to be as high as 997 GPa, with an ultimate strain of 20%. During stretching, the pore size increases, and the graphyne-n sheet becomes progressively weaker. However, the mechanical strength is still significant: a Young's modulus (Y_M) above 500 GPa and an ultimate tensile strength above 40 GPa for graphyne and graphdiyne. High electric field application leads to an accumulation of ions at the interface between the electrolyte and the membrane. Consequently, the membrane was exposed to high stress that can deform the graphyne-n layers, increase pore size, and then decrease the rejection of molecules. For these considerations, graphyne and graphdiyne are also suitable as electrode covers due to their better mechanical properties. These properties are sufficient to meet the requirements for suppressing dendrite growth and maintaining stable cycling performance in lithium-metal batteries.

The analyses of graphyne-n nanostructures before and after deformation through the Radial Distribution Function, g(r), are represented in Fig. S2. The obtained results show that all graphyne-n undergo breaking of bonds and an increase in pore sizes, i.e., an increase in the distance between linkage carbons (see visualizations of the extended monolayers presented in Fig. 6). Analyses of the g(r) curves calculated for all possible pairwise combinations of the acetylenic linkage carbons (C_2) and benzene carbons (C_1) (i.e. C_2–C_2, C_1–C_2, and C_1–C_1) revealed that before the application of tensile stress, the g(r) curves are sharp peaks indicating the ordered structure of graphyne-n. This order is extended to the third neighbor shell in graphyne and graphdiyne, and the second neighbor shell in graphtriyne. Besides, the pairwise separation distances $d(C_1–C_1)$, $d(C_1–C_2)$, and $d(C_2–C_2)$ corresponding to the positions of the first peaks are found to be 1.40 Å, 1.40 Å, and 1.24 Å, respectively. After deformation, the height of the peaks decreases and shifts to the right. This shift is due to the increased distance between the carbons, which are found to be $d(C_1–C_1) = 1.46$ Å, $d(C_1–C_2) = 1.45$ Å, and $d(C_2–C_2) = 1.25$ Å for graphyne, $d(C_1–C_1) = 1.45$ Å, $d(C_1–C_2) = 1.44$ Å, and $d(C_2–C_2) = 1.26$ Å for graphdiyne, and $d(C_1–C_1) = 1.48$ Å, $d(C_1–C_2) = 1.43$ Å, and $d(C_2–C_2) = 1.26$ Å for graphtriyne. All the distances are evaluated within an error of 0.01 Å. We observed that the graphtriyne structure is destroyed under tensile stress. Thus, it is revealed from our study that a graphyne-n with $n > 2$ is inappropriate for electrode protection due to its weak mechanical strength and low ability to reject electrolyte molecules.

Table 2
Summary of the computed mechanical properties of graphyne, graphdiyne, and graphtriyne, compared to graphene.

2D Materials	Y_M (GPa)	Ultimate strength (GPa)	Strain %
		Zigzag	
Graphene	997 1000[a]	127.3 130[a]	24 20[a]
Graphyne	697 700[a]505[c]503.1[d]	112 107.5[a]63.17[c]	30 24.7[d]
Graphdiyne	579 578.6[a]	45.84 45.5[a]	14.7 8[a]
Graphtriyne	464 453.3[a]	33.2 32.5[a]32.3[b]	13.6 9.9[a]19[b]
		Armchair	
Graphene	997 1000[a]	127.3 130[a]	24 20[a]
Graphyne	548 532.5[a]508[c]	39.7 48.2[a]49.78[c]	10 8.2[a]11.2[c]
Graphdiyne	500 469.5[a]	36 36[a]	14 6.3[a]
Graphtriyne	366 365[a]	25.4 26.8[a]31.3[b]	13 7.7[a]12[b]

[a]Results from Ref. [96].
[b]Results from Ref. [95].
[c]Results from Ref. [97].
[d]Results from Ref. [98].

3. Conclusions and remarks

Summarizing our results, we investigated the potential of graphyne-based membranes for protecting battery electrodes using molecular dynamics (MD) and density functional theory (DFT). 2D nanoporous graphyne, graphdiyne, and graphtriyne were considered, and Li^+ cations were passed through the graphyne-n pores with different Li^+ permeability under an applied external electric field. The Li^+ permeability depends on the graphyne-n pore size and the applied electric field. Higher Li^+ permeability was observed for graphtriyne based on both MD and DFT approaches. However, its rejection of electrolyte molecules was low, especially at the high applied electric field (E = 1 V/Å). For graphdiyne, the Li^+ permeability and the rejection of electrolyte molecules were found to be high for an applied electric field up to 0.75

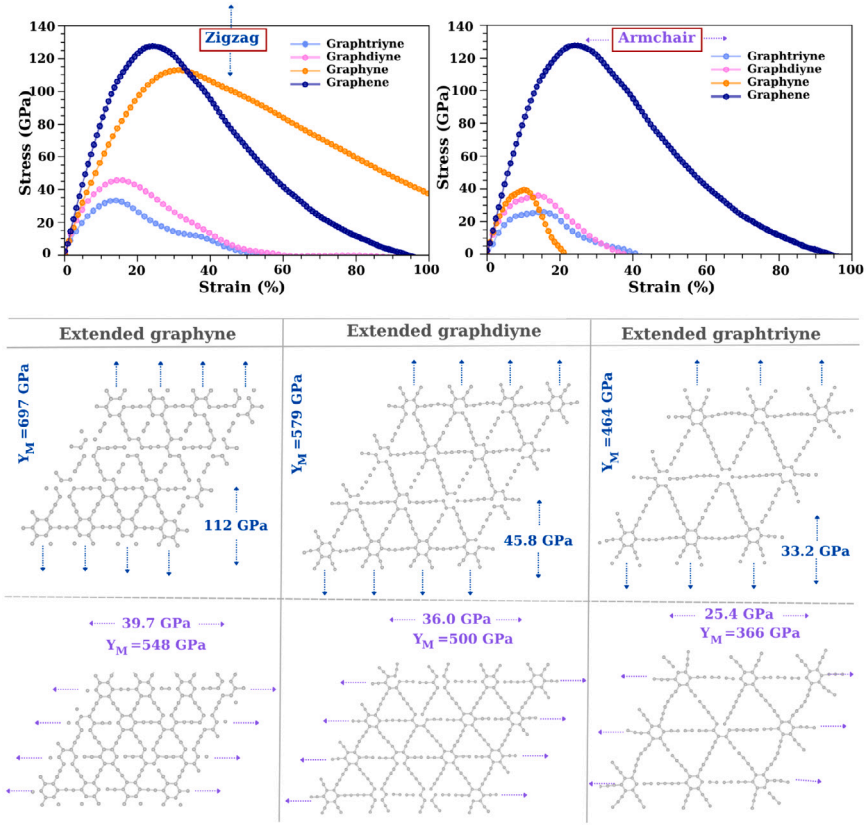

Fig. 6. The uniaxial stress–strain curves and visualizations of the extended monolayers of graphyne, graphdiyne, and graphtriyne.

V/Å. For graphyne, the Li^+ permeability was slightly less than that of graphdiyne and graphtriyne, and 100% electrolyte molecule rejection was achieved for all applied electric fields: E = 0.5 V/Å, E = 0.75 V/Å, and E = 1 V/Å. It was also revealed that the in-plane and out-of-plane Li diffusion barrier profiles are inversely proportional to the triangular pore size. Based on these remarkable thermodynamics and kinetic results, graphyne and graphdiyne membranes are expected to be very promising candidates for Li-battery electrode protection. The small and equally sized, uniformly distributed pores throughout graphyne-n, which have excellent mechanical properties, prevent uneven ion flow and fluctuations in electrode current density. Thus, graphyne-n is supposed to withstand lithium anode dendrite growth. Exhaustive studies on the ability of graphyne-n to suppress dendrite growth and the underlying physical chemistry at the Li-anode/graphyne interface will be the focus of our future research.

4. Methods and computational details

Density function theory calculations

Through our study, we initially performed first-principles calculations within the framework of Density Functional Theory (DFT) as part of the Vienna Ab Initio Simulation Package (VASP) [99]. The generalized gradient approximation in the form of the Perdew Burke Ernzerhof (PBE) functional [100] was adopted self-consistently through the approach of the Projector Augmented Wave (PAW). The Kohn–Sham electron wave functions were expanded with an energy cutoff of 600 eV, and the convergence criteria during the structural optimizations were set to 10^{-6} eV and 10^{-3} eV/Å for energy and force, respectively. The vacuum layer during all the calculations was set to 30 Å in the *z*-direction to prevent interaction between stacked layers and periodic images. The Monkhorst Pack K-point of the 9 × 9 × 1 grid is used in the reciprocal space during the geometrical optimizations [101]. The electron localization function and charge transfer between atoms are assessed on the basis of the Bader charge algorithm [102].

Additionally, the effect of van der Waals interactions during Li adsorption and diffusion was particularly taken into account via the adoption of the empirical scheme of Grimme's semi-empirical adjustments (DFT-D2). The ionic diffusion was examined based on the Climbing-Image Nudged Elastic Band (CI-NEB) scheme [103], which requires the starting and ending positions as inputs and generates a number of intermediate configurations through linear interpolation. Henceforth, the energy barriers between the starting and ending states are calculated by minimizing the energy and atomic forces in all intermediate configurations.

Atomistic molecular dynamics simulations

The electrode/electrolyte interaction that causes the dissociation of electrode and/or electrolyte molecules [104,105] is widely reported. For the purposes of this study, the electrodes are represented by fixed walls for simplicity, as layers of graphyne-n are used to prevent contact between the electrolytes and electrodes. Nevertheless, the battery charge is simulated by the accumulation of cations near the anode region through the application of an external electric field. The application of a high external electric field of up to 1 V/Å also directs the FSI^- counterions to the cathode region, aligns the PVDF polymer chains, and thus allows for rapid diffusion of the ions during an MD simulation of battery charging. From the literature, several reports have used a graphyne-n fixed monolayer for water desalination purposes using MD simulations. However, the synthesis of graphyne-n layers leads to multilayered graphyne-n [106–108]. For proper modeling, we considered four layers of graphyne-n for the AllSSLiB electrode's protection and simulated their dynamics. The GROMOS force field is used for graphyne-n, where the parameters are generated using the Automated Topology Builder [109–111]. The OPLS-AA force field was

used to build the interaction potential models of the PVDF chains and FEC [112–114]. For the ions, the interaction potential parameters were taken from the Canongia Lopes & Padua (CL&P) force field for ionic liquids [115,116]. All MD simulations were conducted using the LAMMPS software package [117]. The visualizations and snapshots of the simulated systems were performed using the three-dimensional visualization system for electronic and structural analysis (VESTA) [118] and Open VIsualization TOol (OVITO) [119]. In the LAMMPS MD simulations, periodic boundary conditions are used for the two dimensions parallel to the graphyne-n layers (x and z directions), and a fixed boundary condition is used for the direction perpendicular to the graphyne-n layers (y direction). A cut-off distance of r_{cut} = 15 Å is used for both Lennard Jones and Coulomb interactions, and a time-step of δt = 1 fs is utilized for all simulated cases. The long-range electrostatic interactions are resolved using the Ewald method [120]. The initial distribution was generated using the Moltemplate package [121]. In this process, the simulated system constituents are placed randomly into a monoclinic box. Then, the system was energetically minimized to correct the bond lengths and ensure optimal particle distribution. The energy minimization algorithm consists of adjusting particle coordinates iteratively [122]. A finite, unitless stopping tolerance for energy (Estop = 10^{-7}) that represents the energy variation between consecutive iterations divided by the energy magnitude, and a stopping tolerance for force (Fstop = 10^{-8} kcal/Å $^{-1}$), are chosen. The equilibrium corresponds to the minimum energy acquired at a short time (t ∼ 0.1 ns) for all simulated cases. After that, the system is agitated using the Langevin thermostat [123] at T = 900 K for another t = 1 ns, followed by the same process using the Nosé-Hoover thermostat [117,123]. Then, to reach the desired ambient condition of temperature and pressure (T = 300 K, P = 1 bar), the simulated systems were equilibrated in the NPT statistical ensemble using the Berendsen barostat [117,124]. Firstly, from T = 900 K to T = 300 K at a constant pressure of P = 500 bar for t = 1 ns. Secondly, the pressure decreases from P = 500 bar to P = 1 bar at a constant temperature of T = 300 K over a time period of t = 1 ns. In the final NPT equilibration stage, the systems were equilibrated at room temperature and ambient pressure (T = 300 K, P = 1 bar) for 10 ns. To study the Li^+ permeability and rejection of other molecules (FSI^-, FEC, PVDF), we conducted simulations in the NVT statistical ensemble using the Nosé-Hoover thermostat at T = 300 K and fixed volume, in the presence of a strong external electric field (E). Three values are considered: E = 0.5 V/Å, E = 0.75 V/Å, and E = 1 V/Å. We confirm that a simulation time of 1 ns under high external electric field application is sufficient for battery charging, since the number of Li^+ ions crossing the graphyne-n multilayer membrane reaches a constant value with slight variation. Finally, from an initial configuration of graphyne-n (n = 0, 1, 2, 3) monolayer equilibrated in the NPT-ensemble, with P = 0 bar and T = 300 K, we performed a uniaxial strain in the zigzag and armchair directions using a strain rate of 1.2×10^{12} s^{-1} to determine Young's modulus from the linear slope of the stress–strain curves and compare the stiffness of graphyne-n [125].

CRediT authorship contribution statement

Mohammed Lemaalem: Conceived the idea, Performed the calculations, Writing – original draft. **Nabil Khossossi:** Conceived the idea, Performed the calculations, Writing – original draft. **Gaelle Bouder:** Contributed to calculations, Writing – original draft. **Poulumi Dey:** Supervision, Writing – original draft. **Philippe Carbonnière:** Conceived the idea, Supervision, Writing – original draft.

Declaration of competing interest

The authors declare that they have no known competing financial interests or personal relationships that could have appeared to influence the work reported in this paper.

Acknowledgments

M.L. and P.C. acknowledge the i-site E2S (Energy and Environment Solutions) of the University of Pau and Pays de l'Adour and the municipalities association of Lacq-Orthez for their financial support (No. CONV-2019-0082) through the HUB project RAISE 2024, the Jülich Supercomputing Centre (JSC) (No. icei-prace-2021-0003), and the TGCC (No. GENCI A0110911484) for providing computational facilities. N.K. and P.D. acknowledge the Dutch Research Council (NWO) Domain Science for the use of supercomputer facilities.

Appendix A. Supplementary data

Supporting electronic information is available.

Supplementary material related to this article can be found online at https://doi.org/10.1016/j.jpowsour.2023.233482.

References

[1] A. Das, S. Sahu, M. Mohapatra, S. Verma, A.J. Bhattacharyya, S. Basu, Lithium-ion conductive glass-ceramic electrolytes enable safe and practical li batteries, Mater. Today Energy (2022) 101118.
[2] Y. Nikodimos, W.-N. Su, B.J. Hwang, Halide solid-state electrolytes: Stability and application for high voltage all-solid-state li batteries, Adv. Energy Mater. (2022) 2202854.
[3] C. Wang, J. Liang, J.T. Kim, X. Sun, Prospects of halide-based all-solid-state batteries: From material design to practical application, Sci. Adv. 8 (36) (2022) eadc9516.
[4] W. Zaman, K.B. Hatzell, Processing and manufacturing of next generation lithium-based all solid-state batteries, Curr. Opin. Solid State Mater. Sci. 26 (4) (2022) 101003.
[5] S. Kundu, Y. Ein-Eli, A review on design considerations in polymer and polymer composite solid-state electrolytes for solid li batteries, J. Power Sources 553 (2023) 232267.
[6] F. Wu, S. Fang, M. Kuenzel, T. Diemant, J.-K. Kim, D. Bresser, G.-T. Kim, S. Passerini, Bilayer solid electrolyte enabling quasi-solid-state lithium-metal batteries, J. Power Sources 557 (2023) 232514.
[7] S. Payandeh, F. Strauss, A. Mazilkin, A. Kondrakov, T. Brezesinski, Tailoring the LiNbO 3 coating of Ni-rich cathode materials for stable and high-performance all-solid-state batteries, Nano Res. Energy 1 (3) (2022) e9120016.
[8] Y. Lu, C.-Z. Zhao, H. Yuan, J.-K. Hu, J.-Q. Huang, Q. Zhang, Dry electrode technology, the rising star in solid-state battery industrialization, Matter 5 (3) (2022) 876–898.
[9] Z. Huang, X. Liu, Y. Zheng, Q. Wang, J. Liu, S. Xu, Boosting efficient and low-energy solid phase regeneration for single crystal LiNi0. 6Co0. 2Mn0. 2O2 via highly selective leaching and its industrial application, Chem. Eng. J. 451 (2023) 139039.
[10] A. Joseph, J. Sobczak, G. Żyła, S. Mathew, Ionic liquid and ionanofluid-based redox flow batteries—A mini review, Energies 15 (13) (2022) 4545.
[11] X. Zhou, H. Zhou, S. Yan, Y. He, W. Zhang, H. Li, K. Wang, K. Jiang, Increasing the actual energy density of sb-based liquid metal battery, J. Power Sources 534 (2022) 231428.
[12] H. Kühnelt, A. Beutl, F. Mastropierro, F. Laurin, S. Willrodt, A. Bismarck, M. Guida, F. Romano, Structural batteries for aeronautic applications—State of the art, research gaps and technology development needs, Aerospace 9 (1) (2022) 7.
[13] F. Liu, Y. Cheng, X. Zuo, R. Chen, J. Zhang, L. Mai, L. Xu, Gradient trilayer solid-state electrolyte with excellent interface compatibility for high-voltage lithium batteries, Chem. Eng. J. 441 (2022) 136077.
[14] L. Li, J. Wang, L. Zhang, H. Duan, Y. Deng, G. Chen, Rational design of a heterogeneous double-layered composite solid electrolyte via synergistic strategies of asymmetric polymer matrices and functional additives to enable 4.5 V all-solid-state lithium batteries with superior performance, Energy Storage Mater. 45 (2022) 1062–1073.
[15] V. Raj, N.P.B. Aetukuri, J. Nanda, Solid state lithium metal batteries–Issues and challenges at the lithium-solid electrolyte interface, Curr. Opin. Solid State Mater. Sci. 26 (4) (2022) 100999.
[16] O.M. Ayoola, A. Buldum, S. Farhad, S.A. Ojo, A review on the molecular modeling of argyrodite electrolytes for all-solid-state lithium batteries, Energies 15 (19) (2022) 7288.
[17] Y.-Y. Sun, Q. Zhang, L. Yan, T.-B. Wang, P.-Y. Hou, A review of interfaces within solid-state electrolytes: fundamentals, issues and advancements, Chem. Eng. J. (2022) 135179.
[18] T. Foroozan, S. Sharifi-Asl, R. Shahbazian-Yassar, Mechanistic understanding of Li dendrites growth by in-situ/operando imaging techniques, J. Power Sources 461 (2020) 228135.

[19] Z. Deng, X. Lin, Z. Huang, J. Meng, Y. Zhong, G. Ma, Y. Zhou, Y. Shen, H. Ding, Y. Huang, Recent progress on advanced imaging techniques for lithium-ion batteries, Adv. Energy Mater. 11 (2) (2021) 2000806.

[20] K.-C. Pu, X. Zhang, X.-L. Qu, J.-J. Hu, H.-W. Li, M.-X. Gao, H.-G. Pan, Y.-F. Liu, Recently developed strategies to restrain dendrite growth of Li metal anodes for rechargeable batteries, Rare Met. 39 (6) (2020) 616–635.

[21] K. Kim, D.J. Siegel, Predicting wettability and the electrochemical window of lithium-metal/solid electrolyte interfaces, ACS Appl. Mater. Interfaces 11 (43) (2019) 39940–39950.

[22] V. Lacivita, Y. Wang, S.-H. Bo, G. Ceder, Ab initio investigation of the stability of electrolyte/electrode interfaces in all-solid-state Na batteries, J. Mater. Chem. A 7 (14) (2019) 8144–8155.

[23] C. Yan, R. Xu, Y. Xiao, J.-F. Ding, L. Xu, B.-Q. Li, J.-Q. Huang, Toward critical electrode/electrolyte interfaces in rechargeable batteries, Adv. Funct. Mater. 30 (23) (2020) 1909887.

[24] X. Zhang, J. Meng, X. Wang, Z. Xiao, P. Wu, L. Mai, Comprehensive insights into electrolytes and solid electrolyte interfaces in potassium-ion batteries, Energy Storage Mater. 38 (2021) 30–49.

[25] S.-F. Wang, H.-C. Lu, Y.-F. Hsu, P. Jasinski, High-performance anode-supported solid oxide fuel cells with co-fired Sm0.2Ce0.8O2-δ/La0.8Sr0.2Ga0.8Mg0.2O3-δ/Sm0.2Ce0.8O2-δ sandwiched electrolyte, Int. J. Hydrogen Energy 47 (8) (2022) 5429–5438.

[26] G.J. Chung, J. Han, S.-W. Song, Fire-preventing LiPF6 and ethylene carbonate-based organic liquid electrolyte system for safer and outperforming lithium-ion batteries, ACS Appl. Mater. Interfaces 12 (38) (2020) 42868–42879.

[27] T. Deng, X. Ji, Y. Zhao, L. Cao, S. Li, S. Hwang, C. Luo, P. Wang, H. Jia, X. Fan, et al., Tuning the anode–electrolyte interface chemistry for garnet-based solid-state Li metal batteries, Adv. Mater. 32 (23) (2020) 2000030.

[28] Z. Shen, W. Zhang, G. Zhu, Y. Huang, Q. Feng, Y. Lu, Design principles of the anode–electrolyte interface for all solid-state lithium metal batteries, Small Methods 4 (1) (2020) 1900592.

[29] Z. Lin, X. Guo, R. Zhang, M. Tang, P. Ding, Z. Zhang, L. Wu, Y. Wang, S. Zhao, Q. Zhang, et al., Molecular structure adjustment enhanced anti-oxidation ability of polymer electrolyte for solid-state lithium metal battery, Nano Energy 98 (2022) 107330.

[30] X. Wang, X. Li, H. Fan, L. Ma, Solid electrolyte interface in Zn-based battery systems, Nano-Micro Lett. 14 (1) (2022) 1–24.

[31] Y. Peng, F. Hao, Mechano-electrochemical coupling in flexible all-solid-state lithium metal batteries, J. Energy Storage 57 (2023) 106195.

[32] N. Sharma, D. Meng, X. Wu, L.S. de Vasconcelos, L. Li, K. Zhao, Nanoindentation measurements of anisotropic mechanical properties of single crystalline NMC cathodes for Li-ion batteries, Extreme Mech. Lett. 58 (2023) 101920.

[33] S.N. Bryntesen, I. Tolstorebrov, A.M. Svensson, P. Shearing, J.J. Lamb, O.S. Burheim, Introducing lignin as a binder material for the aqueous production of NMC111 cathodes for Li-ion batteries, Mater. Adv. (2023).

[34] Y. Li, X. Li, C. Du, H. Sun, Y. Zhang, Q. Liu, T. Yang, J. Zhao, C. Delmas, S.J. Harris, et al., Degradation by kinking in layered cathode materials, ACS Energy Lett. 6 (11) (2021) 3960–3969.

[35] C. Zheng, J. Wu, L. Zhang, H. Wang, Vital roles of fluoroethylene carbonate in electrochemical energy storage devices: a review, J. Mater. Chem. C (2023).

[36] P. Mei, Y. Zhang, W. Zhang, Low-temperature lithium-ion batteries: challenges and progress of surface/interface modifications for advanced performance, Nanoscale (2023).

[37] J. Li, Z. Kong, X. Liu, B. Zheng, Q.H. Fan, E. Garratt, T. Schuelke, K. Wang, H. Xu, H. Jin, Strategies to anode protection in lithium metal battery: a review, InfoMat 3 (12) (2021) 1333–1363.

[38] H. Zhou, H. Zhang, H. Wang, S. Zhang, T. Feng, Z. Xu, Z. Fang, M. Wu, Plasma grown fluoride-rich artificial SEI for stabilizing Li metal anodes, J. Alloys Compd. 935 (2023) 168081.

[39] J. Castillo, J.A. Coca-Clemente, J. Rikarte, A. Sáenz de Buruaga, A. Santiago, C. Li, Recent progress on lithium anode protection for lithium–sulfur batteries: Review and perspective, APL Mater. 11 (1) (2023) 010901.

[40] H. Qian, H. Ren, Y. Zhang, X. He, W. Li, J. Wang, J. Hu, H. Yang, H.M.K. Sari, Y. Chen, et al., Surface doping vs. Bulk doping of cathode materials for lithium-ion batteries: A review, Electrochem. Energy Rev. 6 (1) (2023) 1–32.

[41] M. Wang, F. Zhang, C.-S. Lee, Y. Tang, Low-cost metallic anode materials for high performance rechargeable batteries, Adv. Energy Mater. 7 (23) (2017) 1700536.

[42] L. Qi, Z. Wu, B. Zhao, B. Liu, W. Wang, H. Pei, Y. Dong, S. Zhang, Z. Yang, L. Qu, et al., Advances in artificial layers for stable lithium metal anodes, Chem. Eur. J. 26 (19) (2020) 4193–4203.

[43] B. Zhu, Y. Jin, X. Hu, Q. Zheng, S. Zhang, Q. Wang, J. Zhu, Poly (dimethylsiloxane) thin film as a stable interfacial layer for high-performance lithium-metal battery anodes, Adv. Mater. 29 (2) (2017) 1603755.

[44] Q. Man, Y. An, C. Liu, H. Shen, S. Xiong, J. Feng, Interfacial design of silicon/carbon anodes for rechargeable batteries: A review, J. Energy Chem. (2022).

[45] P. Saha, T.R. Mohanta, A. Kumar, SEI layer and impact on si-anodes for Li-ion batteries, in: Silicon Anode Systems for Lithium-Ion Batteries, Elsevier, 2022, pp. 183–263.

[46] Z. Jiang, A. Li, C. Meng, X. Chen, H. Song, Strategies and challenges of carbon materials in the practical applications of lithium metal anode: a review, Phys. Chem. Chem. Phys. (Incorporating Faraday Trans.) 24 (43) (2022) 26356–26370.

[47] H. Kwon, J. Baek, H.-T. Kim, Building lithium metal batteries under lean electrolyte conditions: challenges and progress, Energy Storage Mater. (2022).

[48] D. Pandel, J. Neises, S.O. Kilian, H. Wiggers, N. Benson, Lithium-ion battery anodes based on silicon nitride nanoparticles as active material and vertically aligned carbon nanotubes as electrically conductive scaffolding, ACS Appl. Energy Mater. (2022).

[49] Y. Pei, Y. Wang, A.-Y. Chang, Y. Liao, S. Zhang, X. Wen, S. Wang, Nanofiber-in-microfiber carbon/silicon composite anode with high silicon content for lithium-ion batteries, Carbon 203 (2023) 436–444.

[50] Z. Liang, C. Peng, J. Shen, Y. Yang, S. Yao, D. Xue, M. Zhu, J. Liu, Lithiophilic single-atom co on carbon nanosheets synergistically modulates Li deposition enable dendrite-free lithium metal batteries, J. Power Sources 556 (2023) 232474.

[51] D. Acharya, I. Pathak, B. Dahal, P.C. Lohani, R.M. Bhattarai, A. Muthurasu, T. Kim, T.H. Ko, K. Chhetri, H.Y. Kim, Immoderate nanoarchitectures of bimetallic MOF derived Ni–Fe–O/NPC on porous carbon nanofibers as freestanding electrode for asymmetric supercapacitors, Carbon 201 (2023) 12–23.

[52] S. Zhang, S. Xiao, D. Li, J. Liao, F. Ji, H. Liu, L. Ci, Commercial carbon cloth: an emerging substrate for practical lithium metal batteries, Energy Storage Mater. (2022).

[53] J. Ryu, D.-Y. Han, D. Hong, S. Park, A polymeric separator membrane with chemoresistance and high Li-ion flux for high-energy-density lithium metal batteries, Energy Storage Mater. 45 (2022) 941–951.

[54] Y. Li, Y. Zhao, Y. Yang, Z. Wang, Q. Yang, J. Deng, Functional separators for long-life and safe Li metal batteries: A minireview, Polymers 14 (21) (2022) 4546.

[55] M. Lemaalem, P. Carbonniere, Tunable properties of poly (vinylidene fluoride)-derived polymers for advancing battery performance and enabling diverse applications, Polymer 283 (2023) 126218.

[56] Y.-H. Lai, C. Rusly, H.-Y. Chen, Regulating solid electrolyte interphase with amide-rich carbon nanotube interlayer for high power lithium-sulfur battery, Surf. Interfaces (2022) 102578.

[57] S. Zhu, J. Ni, The critical role of carbon nanotubes in bridging academic research to commercialization of lithium batteries, Chem. Rec. 22 (10) (2022) e202200125.

[58] S.-Y. Liao, S.-F. Cui, Y.-Z. Li, W.-X. Cheng, X.-W. Huang, J. Zhang, T.-T. Cui, X.-G. Shu, Y.-G. Min, Wrinkled and flexible N-doped MXene additive for improving the mechanical and electrochemical properties of the nickel-rich LiNi0. 8Co0. 1Mn0. 1O2 cathode, Electrochim. Acta 410 (2022) 139989.

[59] L. Ding, N. Yan, S. Zhang, R. Xu, T. Wu, F. Yang, Y. Cao, M. Xiang, Separator impregnated with polyvinyl alcohol to simultaneously improve electrochemical performances and compression resistance, Electrochim. Acta 403 (2022) 139568.

[60] C. Zhou, Q. He, Z. Li, J. Meng, X. Hong, Y. Li, Y. Zhao, X. Xu, L. Mai, A robust electrospun separator modified with in situ grown metal-organic frameworks for lithium-sulfur batteries, Chem. Eng. J. 395 (2020) 124979.

[61] R.H. Baughman, H. Eckhardt, M. Kertesz, Structure-property predictions for new planar forms of carbon: Layered phases containing sp2 and sp atoms, J. Chem. Phys. 87 (11) (1987) 6687–6699.

[62] X. Gao, H. Liu, D. Wang, J. Zhang, Graphdiyne: synthesis, properties, and applications, Chem. Soc. Rev. 48 (2019) 908–936.

[63] Q. Li, Y. Li, Y. Chen, L. Wu, C. Yang, X. Cui, Synthesis of γ-graphyne by mechanochemistry and its electronic structure, Carbon 136 (2018) 248–254.

[64] Y. Song, X. Li, Z. Yang, J. Wang, C. Liu, C. Xie, H. Wang, C. Huang, A facile liquid/liquid interface method to synthesize graphyne analogs, Chem. Commun. 55 (46) (2019) 6571–6574.

[65] C. Yang, Y. Li, Y. Chen, Q. Li, L. Wu, X. Cui, Mechanochemical synthesis of γ-graphyne with enhanced lithium storage performance, Small 15 (8) (2019) 1804710.

[66] Y. Hu, C. Wu, Q. Pan, Y. Jin, R. Lyu, V. Martinez, S. Huang, J. Wu, L.J. Wayment, N.A. Clark, et al., Synthesis of γ-graphyne using dynamic covalent chemistry, Nat. Synth. (2022) 1–6.

[67] M. Barua, A. Saraswat, C. Rao, A novel method for synthesis of γ-graphyne and their charge transfer properties, Carbon 200 (2022) 247–252.

[68] G. Li, Y. Li, H. Liu, Y. Guo, Y. Li, D. Zhu, Architecture of graphdiyne nanoscale films, Chem. Commun. 46 (2010) 3256–3258.

[69] M.M. Haley, S.C. Brand, J.J. Pak, Carbon networks based on dehydrobenzoannulenes: Synthesis of graphdiyne substructures, Angew. Chem., Int. Ed. Engl 36 (8) (1997) 836–838.

[70] H. Zhang, X. He, M. Zhao, M. Zhang, L. Zhao, X. Feng, Y. Luo, Tunable hydrogen separation in sp–sp2 hybridized carbon membranes: a first-principles prediction, J. Phys. Chem. C 116 (31) (2012) 16634–16638.

[71] M. Mehrdad, A. Moosavi, An efficient graphyne membrane for water desalination, Polymer 175 (2019) 310–319.

[72] S. Chandra Shekar, R. Swathi, Rattling motion of alkali metal ions through the cavities of model compounds of graphyne and graphdiyne, J. Phys. Chem. A 117 (36) (2013) 8632–8641.

[73] H. Zhang, M. Zhao, X. He, Z. Wang, X. Zhang, X. Liu, High mobility and high storage capacity of lithium in sp–sp2 hybridized carbon network: the case of graphyne, J. Phys. Chem. C 115 (17) (2011) 8845–8850.

[74] J. Kim, S. Kang, J. Lim, W.Y. Kim, Study of Li adsorption on graphdiyne using hybrid DFT calculations, ACS Appl. Mater. Interfaces 11 (3) (2018) 2677–2683.

[75] Y. Guo, X. Lan, J. Cao, B. Xu, Y. Xia, J. Yin, Z. Liu, A comparative study of the reversible hydrogen storage behavior in several metal decorated graphyne, Int. J. Hydrogen Energy 38 (10) (2013) 3987–3993.

[76] Y. Guo, K. Jiang, B. Xu, Y. Xia, J. Yin, Z. Liu, Remarkable hydrogen storage capacity in Li-decorated graphyne: theoretical predication, J. Phys. Chem. C 116 (26) (2012) 13837–13841.

[77] B. Jang, J. Koo, M. Park, H. Lee, J. Nam, Y. Kwon, H. Lee, Graphdiyne as a high-capacity lithium ion battery anode material, Appl. Phys. Lett. 103 (26) (2013) 263904.

[78] K. Srinivasu, S.K. Ghosh, Graphyne and graphdiyne: promising materials for nanoelectronics and energy storage applications, J. Phys. Chem. C 116 (9) (2012) 5951–5956.

[79] H. Zhang, Y. Xia, H. Bu, X. Wang, M. Zhang, Y. Luo, M. Zhao, Graphdiyne: A promising anode material for lithium ion batteries with high capacity and rate capability, J. Appl. Phys. 113 (4) (2013) 044309.

[80] C. Huang, Y. Li, N. Wang, Y. Xue, Z. Zuo, H. Liu, Y. Li, Progress in research into 2D graphdiyne-based materials, Chem. Rev. 118 (16) (2018) 7744–7803.

[81] C. Huang, S. Zhang, H. Liu, Y. Li, G. Cui, Y. Li, Graphdiyne for high capacity and long-life lithium storage, Nano Energy 11 (2015) 481–489.

[82] S. Zhang, H. Liu, C. Huang, G. Cui, Y. Li, Bulk graphdiyne powder applied for highly efficient lithium storage, Chem. Commun. 51 (10) (2015) 1834–1837.

[83] J. He, K. Bao, W. Cui, J. Yu, C. Huang, X. Shen, Z. Cui, N. Wang, Construction of large-area uniform graphdiyne film for high-performance lithium-ion batteries, Chem. Eur. J. 24 (5) (2018) 1187–1192.

[84] A. Väyrynen, J. Salminen, Lithium ion battery production, J. Chem. Thermodyn. 46 (2012) 80–85.

[85] O. Leonet, L.C. Colmenares, A. Kvasha, M. Oyarbide, A.R. Mainar, T. Glossmann, J.A. Blázquez, Z. Zhang, Improving the safety of lithium-ion battery via a redox shuttle additive 2, 5-Di-tert-butyl-1, 4-bis (2-methoxyethoxy) benzene (DBBB), ACS Appl. Mater. Interfaces 10 (11) (2018) 9216–9219.

[86] V. Ponce, D.E. Galvez-Aranda, J.M. Seminario, Analysis of an all-solid state nanobattery using molecular dynamics simulations under an external electric field, Phys. Chem. Chem. Phys. 23 (1) (2021) 597–606.

[87] R. Parida, S. Pahari, M. Jana, Introducing the potency of new boron-based heterocyclic anion receptor additives to regulate the solvation and transport properties of Li-ions in ethylene carbonate electrolyte of Li-Ion battery: An atomistic molecular dynamics study, J. Power Sources 521 (2022) 230962.

[88] G. Li, Y. Li, H. Liu, Y. Guo, Y. Li, D. Zhu, Architecture of graphdiyne nanoscale films, Chem. Commun. 46 (19) (2010) 3256–3258.

[89] H. Du, H. Yang, C. Huang, J. He, H. Liu, Y. Li, Graphdiyne applied for lithium-ion capacitors displaying high power and energy densities, Nano Energy 22 (2016) 615–622.

[90] N. Khossossi, W. Luo, Z. Haman, D. Singh, I. Essaoudi, A. Ainane, R. Ahuja, Revealing the superlative electrochemical properties of o-B2N2 monolayer in Lithium/Sodium-ion batteries, Nano Energy 96 (2022) 107066.

[91] N. Khossossi, D. Singh, W. Luo, R. Ahuja, Flexible 3D porous boron nitride interconnected network as a high-performance Li-and Na-ion battery electrodes, Electrochim. Acta 421 (2022) 140491.

[92] X. Fan, W. Zheng, J.-L. Kuo, D.J. Singh, Adsorption of single Li and the formation of small Li clusters on graphene for the anode of lithium-ion batteries, ACS Appl. Mater. Interfaces 5 (16) (2013) 7793–7797.

[93] A. Banerjee, N. Khossossi, W. Luo, R. Ahuja, Promise and reality of organic electrodes from materials design and charge storage perspective, J. Mater. Chem. A (2022).

[94] Z. Hao, Q. Zhao, J. Tang, Q. Zhang, J. Liu, Y. Jin, H. Wang, Functional separators towards the suppression of lithium dendrites for rechargeable high-energy batteries, Mater. Horiz. 8 (1) (2021) 12–32.

[95] S. Lin, M.J. Buehler, Mechanics and molecular filtration performance of graphyne nanoweb membranes for selective water purification, Nanoscale 5 (23) (2013) 11801–11807.

[96] S.W. Cranford, D.B. Brommer, M.J. Buehler, Extended graphynes: simple scaling laws for stiffness, strength and fracture, Nanoscale 4 (24) (2012) 7797–7809.

[97] Y.Y. Zhang, Q.X. Pei, C.M. Wang, Mechanical properties of graphynes under tension: A molecular dynamics study, Appl. Phys. Lett. 101 (8) (2012) 081909.

[98] J. Zhao, N. Wei, Z. Fan, J.-W. Jiang, T. Rabczuk, The mechanical properties of three types of carbon allotropes, Nanotechnology 24 (9) (2013) 095702.

[99] G. Kresse, J. Furthmüller, Efficient iterative schemes for ab initio total-energy calculations using a plane-wave basis set, Phys. Rev. B 54 (16) (1996) 11169.

[100] J.P. Perdew, K. Burke, M. Ernzerhof, Generalized gradient approximation made simple, Phys. Rev. Lett. 77 (18) (1996) 3865.

[101] H.J. Monkhorst, J.D. Pack, Special points for brillouin-zone integrations, Phys. Rev. B 13 (12) (1976) 5188.

[102] G. Henkelman, A. Arnaldsson, H. Jónsson, A fast and robust algorithm for bader decomposition of charge density, Comput. Mater. Sci. 36 (3) (2006) 354–360.

[103] G. Henkelman, B.P. Uberuaga, H. Jónsson, A climbing image nudged elastic band method for finding saddle points and minimum energy paths, J. Chem. Phys. 113 (22) (2000) 9901–9904.

[104] Z. Piao, R. Gao, Y. Liu, G. Zhou, H.-M. Cheng, A review on regulating li+ solvation structures in carbonate electrolytes for lithium metal batteries, Adv. Mater. (2022) 2206009.

[105] K. Guo, S. Qi, H. Wang, J. Huang, M. Wu, Y. Yang, X. Li, Y. Ren, J. Ma, High-voltage electrolyte chemistry for lithium batteries, Small Sci. 2 (5) (2022) 2100107.

[106] J.M. Gottfried, Synthesizing a nanographyne, Chem 8 (10) (2022) 2581–2583.

[107] F. Yao, W. Wang, H. Shi, Z. Xu, M. Zeng, Y. Hu, L. Liu, X. Ji, Graphynes: Electronic properties, synthesis, and applications in catalysis, ACS Catal. 11 (22) (2021) 14122–14147.

[108] V.G. Desyatkin, W.B. Martin, A.E. Aliev, N.E. Chapman, A.F. Fonseca, D.S. Galvão, E.R. Miller, K.H. Stone, Z. Wang, D. Zakhidov, et al., Scalable synthesis and characterization of multilayer γ-graphyne, new carbon crystals with a small direct band gap, J. Am. Chem. Soc. 144 (39) (2022) 17999–18008.

[109] A.K. Malde, L. Zuo, M. Breeze, M. Stroet, D. Poger, P.C. Nair, C. Oostenbrink, A.E. Mark, An automated force field topology builder (ATB) and repository: version 1.0, J. Chem. Theory Comput. 7 (12) (2011) 4026–4037.

[110] M. Stroet, B. Caron, K.M. Visscher, D.P. Geerke, A.K. Malde, A.E. Mark, Automated topology builder version 3.0: Prediction of solvation free enthalpies in water and hexane, J. Chem. Theory Comput. 14 (11) (2018) 5834–5845.

[111] K.B. Koziara, M. Stroet, A.K. Malde, A.E. Mark, Testing and validation of the Automated Topology Builder (ATB) version 2.0: prediction of hydration free enthalpies, J. Comput. Aided Mol. Des. 28 (3) (2014) 221–233.

[112] M. Yabe, K. Mori, K. Ueda, M. Takeda, Development of PolyParGen software to facilitate the determination of molecular dynamics simulation parameters for polymers, J. Comput. Chem. Japan-Int. Ed. 5 (2019) 2018–0034.

[113] L.S. Dodda, I. Cabeza de Vaca, J. Tirado-Rives, W.L. Jorgensen, LigParGen web server: an automatic OPLS-AA parameter generator for organic ligands, Nucleic Acids Res. 45 (W1) (2017) W331–W336.

[114] M. Lemaalem, P. Carbonniere, Effects of solvents on li+ distribution and dynamics in pvdf/lifsi solid polymer electrolytes: an all-atom molecular dynamics simulation study, Solid State Ion. 399 (2023) 116304.

[115] J.N. Canongia Lopes, A.A. Pádua, CL&P: A generic and systematic force field for ionic liquids modeling, Theor. Chem. Acc. 131 (3) (2012) 1–11.

[116] K. Goloviznina, Z. Gong, A.A. Padua, The CL &Pol polarizable force field for the simulation of ionic liquids and eutectic solvents, Wiley Interdiscip. Rev. Comput. Mol. Sci. 12 (3) (2022) e1572.

[117] A.P. Thompson, H.M. Aktulga, R. Berger, D.S. Bolintineanu, W.M. Brown, P.S. Crozier, P.J. in't Veld, A. Kohlmeyer, S.G. Moore, T.D. Nguyen, et al., LAMMPS-a flexible simulation tool for particle-based materials modeling at the atomic, meso, and continuum scales, Comput. Phys. Comm. 271 (2022) 108171.

[118] K. Momma, F. Izumi, VESTA: a three-dimensional visualization system for electronic and structural analysis, J. Appl. Crystallogr. 41 (3) (2008) 653–658.

[119] A. Stukowski, Visualization and analysis of atomistic simulation data with OVITO–the Open Visualization Tool, Modelling Simul. Mater. Sci. Eng. 18 (1) (2009) 015012.

[120] W.M. Brown, A. Kohlmeyer, S.J. Plimpton, A.N. Tharrington, Implementing molecular dynamics on hybrid high performance computers–Particle–particle particle-mesh, Comput. Phys. Comm. 183 (3) (2012) 449–459.

[121] A.I. Jewett, D. Stelter, J. Lambert, S.M. Saladi, O.M. Roscioni, M. Ricci, L. Autin, M. Maritan, S.M. Bashusqeh, T. Keyes, et al., Moltemplate: A tool for coarse-grained modeling of complex biological matter and soft condensed matter physics, J. Mol. Biol. 433 (11) (2021) 166841.

[122] J. Guénolé, W.G. Nöhring, A. Vaid, F. Houllé, Z. Xie, A. Prakash, E. Bitzek, Assessment and optimization of the fast inertial relaxation engine (fire) for energy minimization in atomistic simulations and its implementation in lammps, Comput. Mater. Sci. 175 (2020) 109584.

[123] A. Dequidt, J. Devemy, A.A. Padua, Thermalized drude oscillators with the LAMMPS molecular dynamics simulator, J. Chem. Inf. Model. 56 (1) (2016) 260–268.

[124] T.J. Barrett, M.L. Minus, Thermostat, barostat, and damping parameter impact on the tensile behavior of graphene, 2023, Available at SSRN 4289377.

[125] S. Pathak, S.R. Kalidindi, Spherical nanoindentation stress–strain curves, Mater. Sci. Eng.: R: Rep. 91 (2015) 1–36.